GAIA-CLIM deliverable D1.5

Gap Analysis for Integrated Atmospheric ECV CLImate Monitoring:

Modelling studies of the impacts of gaps

Summary of initial model-based study results and plans for remainder of project

A Horizon 2020 project; Grant agreement: 640276

Date: June 2016

Lead Beneficiary: KIT

Nature: R

Dissemination level: PU

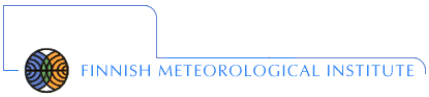

Table of Contents

1. Introduction

This report presents first results from the model-based assessment of the impacts of gaps in observing system current non-satellite measurement capabilities. By making first results available during the course of the task, we hope to gain insights of the possible impacts of these gaps and build upon our knowledge of and ability to characterize the quality of EO measurements through further collaboration within and across this task group and work package (WP). This report is organized by the contributions of each of the groups involved. In Section 2, we briefly summarize key questions and related contributions by each group. For each contribution, we briefly outline the approach used, including a description of the model system applied, and present and discuss the results achieved so far, together with an outlook of next steps as part of this task in Section 3. Overall conclusions to date and recommendations for future activities are given in Section 4.

2. Background

As outlined in our previous report on Modelling Studies of the Impacts of Gaps (GAIA-CLIM Deliverable Report D1.2), this model based assessment of gaps in observing system capabilities complements and extends the remaining activities within GAIA-CLIM work package 1 by addressing questions such as:

- Where the in-situ capabilities are noted to have gaps, or to lack a transfer standard, then do these need to be filled by additional in-situ data, or is a model-based interpolation or analysis based field estimate a plausible alternative means of EO sensor characterisation?
- Where, based upon our understanding of atmospheric processes, would additional measurements add most interpretative value to EO sensor characterisation?
- Does measurement frequency, scheduling or quality matter more? What would be the trade-off between these in terms of our ability to characterise EO sensor performance?
- Do fewer measurements in fewer locations with lower uncertainties have benefits over more measurements at more locations but with higher uncertainties?

Within the planned work of Task 1.5 there is a clear emphasis on the first two questions. Ultimately, progress in Task 1.5 may enable us to also address the last two questions, but this is less clear at present.

In line with the GAIA-CLIM Gap Assessment and Impacts Document (GAID) we categorize known gaps into seven generic gap types:

- coverage (spatiotemporal)
- vertical resolution (profile, per troposphere/stratosphere altitude domain)
- uncertainty (per observation, uncertainty budget, calibration)
- uncertainty (in relation to comparator measures, representativeness)

- technical (formats, conventions etc)
- governance (harmonisation procedures, 24/7, etc)
- parameter (need for auxiliary information/parameters).

In order to meet these project goals specified in the preceding paragraphs, a number of modelling groups, each representing expertise in a key area relevant for GAIA-CLIM, have been incorporated into Task 1.5 activities. The groups involved and model systems used have been selected to cover a wide range of topics and GAIA-CLIM target ECVs, including experts in greenhouse gas modelling, air quality and inversion modelling, aerosol modelling and chemistry climate modelling. Each of the groups is actively involved in further international modelling activities (e.g., such as the WCRP-SPARC / IGAC Chemistry Climate Modelling Initiative, CCMI).

- Max Planck Institute for Biogeochemistry contributes with their expertise in modelling of greenhouse gases (CO_2 and CH_4) and inverse modelling.
- Likewise, BIRA contribute with modelling of air quality and short lived climate forcing gases (in particular CO) and inverse modelling of their sources and sinks, such as investigation of the hydroxyl radical (OH) as a sink for CO.
- FMI contribute with aerosol climate modelling and KIT with chemistry climate modelling to address the climate impact on ozone and related trace gases.
- More recently, ECMWF started work on addressing gaps in geographical coverage of temperature and humidity observations by analyzing the observations minus short term forecast (O-B) statistics.
- A specific (in kind) KNMI contribution to this WP is to pass through the latest relevant information on validation results from MACC/CAMS which are documented in 3-monthly MACC/CAMS validation reports published here http://atmosphere.copernicus.eu/validation.

In terms of the gap type characterization, most of the modelling work within this task addresses gaps in coverage and representativeness, as well as gaps in available parameters, e.g. with respect to multivariate dependencies.

3. Definition of model simulations and preliminary results

In this section, the model simulations that either have been or are to be performed or used are described, together with an outline of the specific analyses to date / foreseen. The presentation is organized by the topics to be addressed, together with the specific model systems to be used: (1) Greenhouse gases CO_2 and CH_4, (2) air quality and short lived climate forcing gases (CO), (3) aerosols, (4) ozone and related trace gases and (5) assessing geographical gaps for reference temperature and humidity. Table 1 summarizes the topics addressed and models involved, including an additional model, (5) from the previous modelling study of the impacts of gaps as part of GAIA-CLIM D1.2.

Table 1: Updated topics addressed in Task 1.5 by specific models, the respective ground-based observational networks addressed, and the institutions responsible for this part of the work.

	Model	*Technique*	*Network addressed*	*Institution*
Greenhouse gases, CO_2, CH_4	**TM3**	**Global tracer transport model**	**TCCON**	**MPI BGG**
Air quality, CO	**IMAGESv2**	**Inverse modelling**	**TCCON**	**BIRA**
Aerosols	**ECHAM-HAMMOZ**	**Aerosol Climate model**	**AERONET**	**FMI**
Ozone and related trace gases	**EMAC (ECHAM5-MESSy2)**	**Chemistry Climate model**	**NDACC**	**KIT**
Temperature and humidity	**ECMWF IFS**	**Numerical Weather Prediction**	**GRUAN**	**ECMWF**

3.1 Greenhouse gases, CO_2 and CH_4 (MPI BGC)

3.1.1 Scope of the assessment

TCCON (Total Carbon Column Observing Network, see Wunch et al., 2011), a distributed network of ground-based Fourier Transform Infrared (FTIR) spectrometers, is currently the backbone of the validation of spaceborne column-integrated measurements of carbon dioxide and methane (hereafter XCO_2 and XCH_4, respectively). The locations of the TCCON sites are shown in Figure 1.1. This assessment attempts to quantify over what spatial and temporal scales these measurements are representative of the atmospheric composition through the use of sophisticated collocation criteria using modelled fields to represent variability due to both transport and fluxes, following the approach of Guerlet et al. (2013). Furthermore, these colocation criteria are applied to GOSAT retrievals to assess how well the TCCON-GOSAT colocations sample the geophysical parameter space that constitutes the basis of the currently implemented bias correction schemes.

The first part of this study defines the representativeness of the validation network in space and time, which addresses the first gap type listed in Section 2, with the region of representativeness influenced by the uncertainty on the measurements, which is related to the fourth gap type. The second part of the study, the analysis in parameter space, relates to the seventh gap type listed.

Figure 1.1. The location of past, current, and planned TCCON sites, as of 2014. Only operational and sites marked as "future sites" are considered in this analysis.

3.1.2 Model used and planned simulations

The original plan had been to use forward simulations of the TM3 tracer transport model at 1.125 degree resolution. This is a higher resolution than that at which we are able to optimize our fluxes through atmospheric inversion (typically carried out at ~4 x 5 degree resolution), so this would have involved some mismatch between the scales of the fluxes and the scale of the transport. Because of this, we opted to instead use optimized 3D fields of carbon dioxide and methane at 1 degree spatial, 3-hourly temporal resolution that are available through the Copernicus Atmosphere Monitoring Service for this study. These runs are performed using the Integrated Forecasting System (IFS) (Agustí-Panareda et al. 2014, S. Massart et al. 2014), a comprehensive, state of the art numerical weather prediction (NWP) and earth-system model developed at the European Centre for Medium Range Weather Forecasts (ECMWF). It models the dynamics of the atmosphere and the physical processes that influence the weather, including atmospheric composition, in addition, it uses data assimilation in order to make better predictions about the state of the atmosphere.

3.1.3 Planned analysis

The collocation method used to determine the region of representativeness around each TCCON site is based on Guerlet et al. (2013). This is done by analysing the optimized fields of XCO_2 (and XCH_4) at 1 degree resolution, and determining regions over which the total column value is not expected to vary more than a given threshold amount (e.g. ±0.5 ppm for XCO_2). What is important to note, is that the exact value of the modelled field is not critical, and the value measured and the value modelled are not directly compared. Rather, the variability of the modelled field is assessed. This takes into account variability related to the heterogeneity of the fluxes in the near-field and the impact this has on the total column, as well as synoptic variability through transport.

An example is shown for the TCCON station at Bialystok in Figure 1.2. The upper left panel shows the simulated XCO_2 fields for one three-hourly timestep within the geographic range ±7.5 degrees latitude, ±22.5 degrees longitude. The upper right shows all the regions that

match the simulated XCO2 value at Bialystok within the ±0.5 ppm threshold, and the lower left shows the effect of filtering such that the matches are contiguous. The lower right panel shows the normalized cumulative matches for one full month, in this case April 2010, where a value of one implies that the value matched for all time steps throughout the month.

This method defines the spatial representativeness of the TCCON network. These "potential colocation" regions are then confronted with GOSAT measurements from 2010, and the soundings are sorted into those that are potentially collocated with the area of influence of the TCCON network and those that are not. The representativeness of the colocations in terms of the geophysical parameters used for empirical bias correction is then assessed. Table 1.1 presents a sampling of some of the geophysical parameters that have been used for empirical bias corrections for various satellite XCO_2 retrieval products.

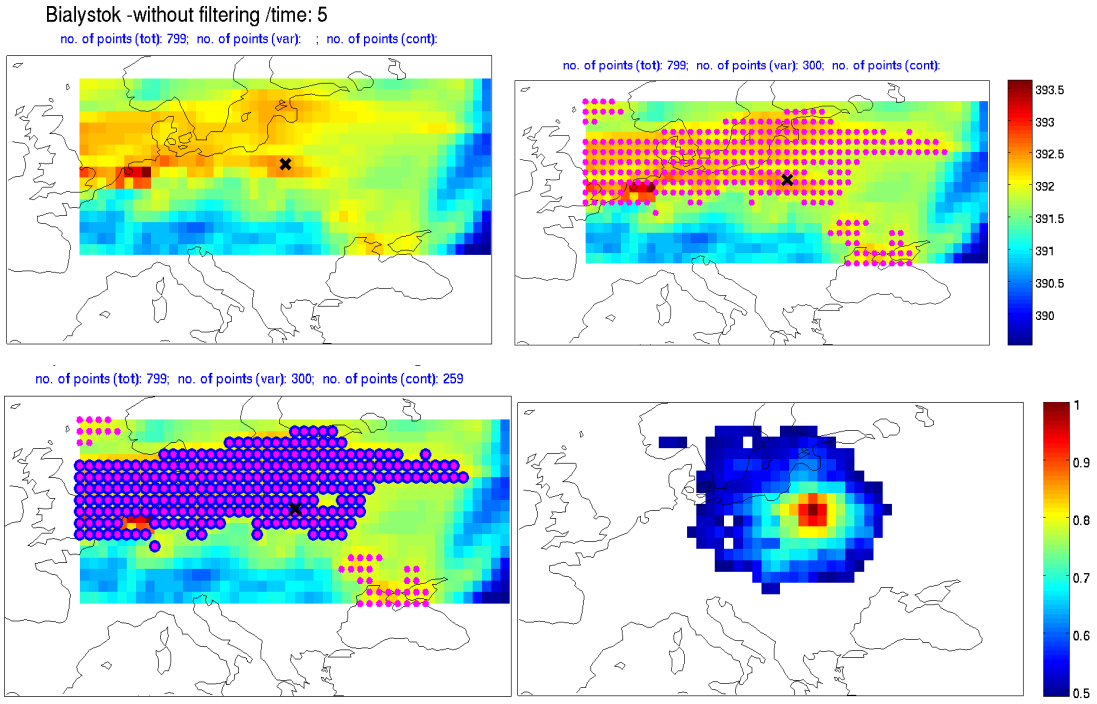

Figure 1.2. A step-by-step example of the colocation method based on Guerlet et al. (2013). The upper left panel shows the modelled XCO_2 field for ±7.5 degrees latitude and ±22.5 degrees longitude around Bialystok. The upper right shows all pixels that match the value at the TCCON site within 0.5 ppm, and the lower left imposes the criterion that all matches must be contiguous in space. The lower right panel shows the normalized fluxes over one month (April, 2010).

Table 1.1. A selection of XCO_2 retrievals and the geophysical parameters (not defined here) which have been empirically found to be significant for multivariate bias corrections.

Sensor	Retrieval	Version	Parameters used
SCIAMACHY	BESD	2.01.01	Albedo_P0_O2, albedo_P0_CO2, albedo_P1_CO2, albedo_P2_CO2, FWHM_CO2 (nm), CWP, APS, Δps, height, SZA, SVA
TANSO (GOSAT)	SRFP	2.3.7	Retrieved aerosol size parameter α
TANSO (GOSAT)	OCFP	6.1	SZA, albedo_band_1/albedo_band_3
TANSO (GOSAT)	ACOS	2.9	"blended_albedo", Δps, airmass, signal_O2
TANSO (GOSAT)	ACOS	3.3	Signal_strong_co2/signal_o2
TANSO (GOSAT)	ACOS	3.4	Δps, albedo_band_2, signal_strong_co2/ signal_weak_co2, zero_level_offset_o2, albedo_slope_strong_co2
OCO-2	ACOS	7	Δps, CO2_grad_del, log(dust, water, salt aerosol)

3.1.4 Current results

The regions of representativeness were determined for each three-hour time step for both XCO_2 and XCH_4. The results did not vary greatly between the two gases, due to correlated anthropogenic fluxes and the dominance of transport as an influencing factor. As such, only the results for XCO_2 are discussed here. Note that the actual sampling of the instrument was not included at this point: only the location was considered, and as such, both night and day are included, as well as conditions of cloud and instrument malfunction. Thus, these are certainly overestimations, especially for very high latitudes, winter conditions, and regions with persistent clouds. Nonetheless, it provides some interesting information about the influence of fluxes vs. transport on the spatial representativeness of a given total column measurement.

Two months are shown in Figure 1.3: April and August 2010. Beginning in the north, it can be seen that the Arctic sites have rather large areas of representativeness for both months, indicating that the variability of the XCO2 fields in space is not tremendously large. Nonetheless, the representativeness is less in August, due to a larger influence of biosphere fluxes. This is more clearly seen for most of the terrestrial mid-latitude sites, which seem to almost disappear in the plot for August: Their areas of representativeness shrink down to only a pixel or two. This is not the result of changing anthropogenic fluxes, but rather the larger gradients brought about by biospheric uptake combined with increased convective transport in the summer months. The ocean-influenced site Izaña is notably less sensitive to this seasonal difference.

In the tropics the site at Manaus (since discontinued) is remarkable for its small area of representativeness over all months, despite being located more or less in the middle of the Amazon. This seems to be largely the result of sampling downwind of the city of Manaus, combined with the variable natural fluxes (biosphere and biomass burning). In general, the sites with a strong influence from oceanic fluxes had rather large regions of

representativeness throughout the year, as is seen at, for example, Lauder, Réunion, and Wollongong. Interestingly the same cannot be said for Ascension Island, despite its location in the middle of the tropical Atlantic. It seems that here the impact of fire plumes from Africa (seen in both the northern and southern burning seasons) as well as the interhemispheric gradient across the intertropical convergence zone restrict the region of representativeness more than one might expect.

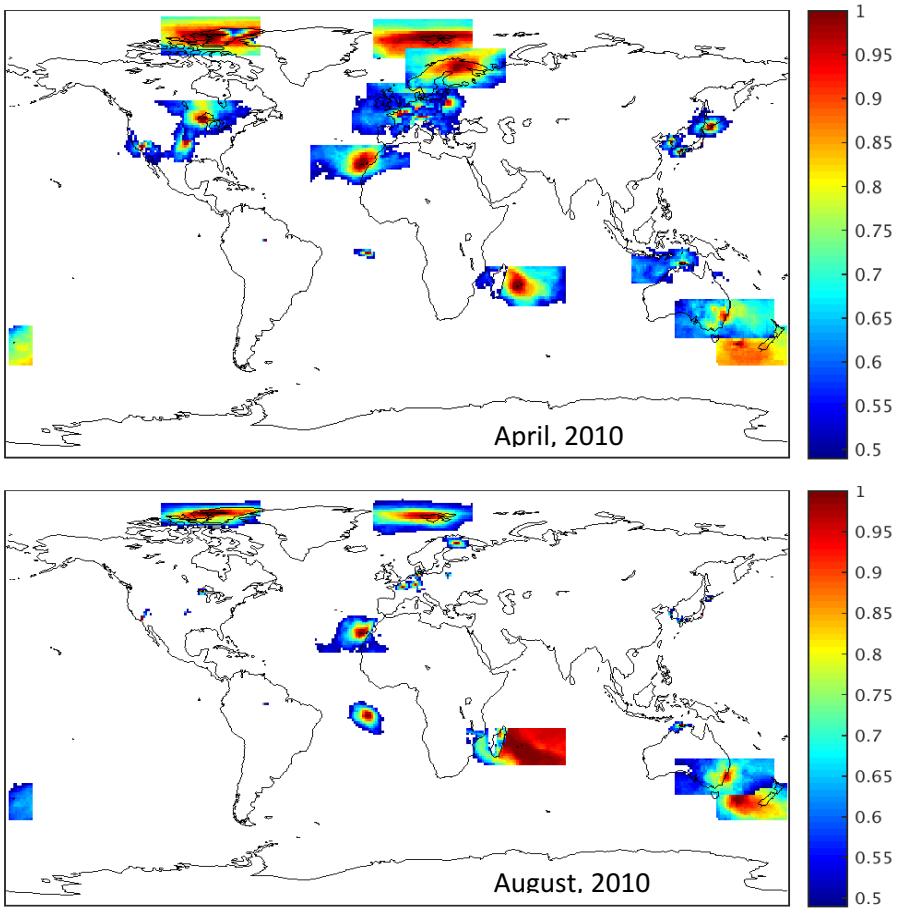

Figure 1.3. The regions of normalized representativeness or potential colocation for XCO_2 are shown for April (upper) and August (lower), 2010. Of interest is how small the colocation regions at the northern midlatitudes become during the convectively active and high photosynthetic uptake month of August, as well as the very small region of representativeness of Manaus, in the Amazon, which is influenced by both local fires and the nearby city of Manaus. The XCH_4 colocation regions are not appreciably different. In contrast, the Arctic, ocean, and Southern Hemisphere sites have generally larger regions of representativeness, as one would expect.

As for the application in parameter space, some results are shown in Figure 1.4. All results shown here are for the SRFP 2.3.7 GOSAT retrieval. Beginning with latitude (top panel) as a sort of bridge between the spatial domain and parameter space, where it can be seen that there are almost no colocations between the latitudes of 0 and 20 degrees north. While there is also a minimum in the number of GOSAT soundings at these latitudes, mostly due to persistent clouds in the tropics, there are no collocated validation measurements at all. The next parameter shown is the surface albedo for Band 2 (~1.6 microns, middle panel of Figure 1.4). Here the coverage is rather good across the parameter space, with only very few

soundings over the very brightest surfaces (albedo > 0.65) being not represented by the validation measurements. The bottom panel shows the retrieved aerosol optical depth for the same band, and again rather good coverage is shown with the TCCON colocations. Here, the peak is skewed to slightly lower AOD, but almost the full range of values is covered.

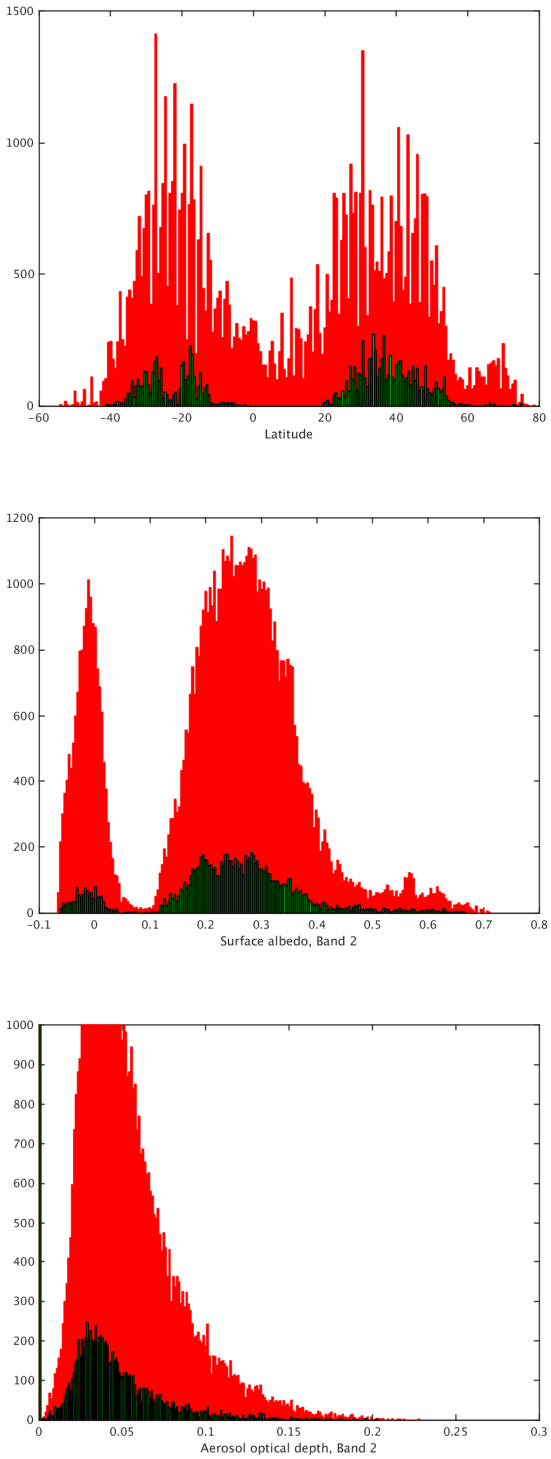

Figure 1.4. All GOSAT SRFP soundings for 2010 are shown in red, those colocated with TCCON are shown in dark green. Three parameters are considered here: latitude, retrieved surface albedo for Band 2, and retrieved aerosol optical depth for Band 2.

3.1.5 Conclusions and future activities

From this analysis, thus far, it can be seen that some stations are clearly representative of a much larger region than others, and their representativeness varies through the year, likely due to the impact of seasonally varying fluxes and transport changes across different seasons. Even though there are far more sites in the northern hemisphere, during the summer months the region of representativeness provided by these measurements is actually rather small. As such, the few Tropical and Southern Hemisphere sites represent a significantly larger region than the comparatively dense network of sites in Europe, North America, and East Asia.

This work will be improved over the next year by considering the actual sampling of the sites, which will more realistically account for the restrictions on observational sampling by FTIR arising due to clouds, solar zenith angle, and instrument downtime. This will also benefit the parameter space analysis.

The parameter space analysis shows that, for many parameters, good coverage is already attained. What still needs to be expanded is the multivariate analysis. For example, Northern Africa is a region that has proved consistently difficult for the retrieval of XCO_2, with all sensors and retrievals reporting values that are considered to be too high. This may be the result of the combination of high aerosol load and high albedo, both of which reach rather extreme values in this region. Figure 1.4 showed that the TCCON sites provided some coverage even at very high albedo and aerosol conditions, but in general there was a gap in this latitude range (0-20 degrees). A multivariate parameter analysis , planned for the next year of the project, will assess how well the simultaneous conditions of high surface albedo and high AOD (for example) are covered, perhaps taking into account solar zenith angle as well. The future work will further develop this analysis along these lines.

3.2 Air quality, carbon monoxide (BIRA)

3.2.1 Scope of the assessment

This part of the study addresses the use of atmospheric measurements of carbon monoxide (CO) to provide constraints on the budget (sources *and* sinks) of this compound. The sources of CO are either direct, due to incomplete combustion, and include fossil fuel, biofuel and vegetation fire burning, or secondary chemical production resulting from the oxidation of hydrocarbons. The dominant CO sink is its reaction with the hydroxyl radical (OH), and therefore CO plays a key role in the oxidative capacity of the atmosphere, and in the removal of air pollutants. In several previous modelling studies, ground-based measurements (CMDL, now GMD) and/or satellite data (MOPITT, AIRS, IASI etc.) have been used in conjunction with global Chemical Transport Models (CTMs) to provide top-down constraints on the surface emissions and (in some cases) also the photochemical production of CO. In such studies, a set of emission parameters (with their specified error covariances) are varied in a CTM in order to reproduce a given set of atmospheric measurements to within their uncertainties. The resulting updated emissions prove to be sensitive not only to the choice of atmospheric dataset (e.g. ground-based vs. satellite) and inversion setup (e.g. number of emission parameters, assignment of errors on emissions and on the measurement data, choice of

either fixed or variable photochemical production due to hydrocarbon oxidation) but they are also greatly influenced by the representation of the chemical sink of CO, i.e. the abundance of hydroxyl radicals (OH). For example, as average OH levels are likely overestimated by most models in the Northern Hemisphere according to analyses of methyl chloroform (MCF) observations, for reasons that remain unclear, the total hemispheric top-down CO emissions are likely too high. Based on MCF observations from surface measurement networks and airborne campaigns, a recent study (Patra et al., 2014) reported an annual ratio of Northern Hemispheric to Southern Hemispheric (NH/SH) OH concentration of 0.97±0.12, very close to 1, and much lower than the ACCMIP multi-model mean (NH/SH) OH ratio estimated at 1.28±0.10 (Naik et al., 2012). The potential impact of uncertainties in OH fields was evaluated in a recent regional-scale study (Jiang et al., 2015) employing the multi-spectral version 5 (V5J) of MOPITT retrievals, in which radiances in the thermal infrared (TIR, 4.7 µm) are combined with radiances in the near infrared (NIR, 2.3 µm), thus providing greater sensitivity to near- surface CO over the main source regions (Worden et al., 2010).

In Task 1.5, it is planned to take advantage of recently published literature in order to address the issue of assessing the CO budget on the global scale and evaluate how ground-based measurements could provide useful constraints in the derivation of top-down emission estimates. To this end, we will use MCF-derived constraints on OH fields from the recent literature (Patra et al., 2014), and based on their uncertainties we shall perform sensitivity source inversions using either MOPITT (Deeter et al., 2013) or IASI CO (George et al., 2015) retrievals for one complete year. Vertical CO profile measurements by ground-based FTIR instruments are used as additional constraints in the source optimizations, since vertical concentration gradients reflect the effects of chemical sinks. Vertical FTIR data are scarce, but better characterized than vertical information from satellites. The latter could, however, be used in a next step.

3.2.2 Model used and planned simulations

The IMAGESv2 global chemistry-transport model (Stavrakou et al., 2015) is to be used in an inverse modelling framework based on its full adjoint model (Müller et al., 2005; Stavrakou and Müller, 2006). This model will be run at 2°x2.5° horizontal resolution with 40 vertical hybrid levels, using ECMWF ERA-Interim meteorology. A priori emissions include vegetation fires from the GFED4 emission inventory (Giglio et al., 2013), isoprene fluxes from the MEGAN-MOHYCAN model (Stavrakou et al., 2014) and fluxes of other biogenic VOC from MEGAN model (Guenther et al., 2012) , and the EDGARv4.2 inventory for global anthropogenic emissions combined with a blend of regional inventories (Bauwens et al., 2016). The chemical mechanism is comprehensive, with more than 120 compounds and a detailed chemical mechanism in particular for isoprene oxidation.

3.2.3 Planned analysis

The following steps are foreseen:

S1. Forward simulation using IMAGESv2, in order to generate a distribution of OH concentrations, $[OH]_{model}$ (4-d distribution, month x latitude x longitude x vertical

level). Then use constraints based on MCF from the literature, namely the global MCF lifetime and the interhemispheric OH ratio. The $[OH]_{model}$ will be scaled to match those constraints, resulting in a best estimate of OH field $[OH]_{best}$, but also a range based on the uncertainties on the constraint.

S2. Using the [OH] uncertainty range, define a set of regular model inversions of CO source, using a methodology similar to Stavrakou and Müller (2006), constrained by satellite (MOPITT, IASI) CO measurements. The inversion involves the minimization of a cost function, which quantifies the overall difference between model and observations, and includes a regularization term penalizing those solutions too different from the a priori.

S3. Perform a series of sensitivity inversions using different OH fields obtained in the previous step (S2). The sensitivity inversions will provide an ensemble of CO fields (month x latitude x longitude x vertical level), which minimize the difference between the model and the observations within the given uncertainties.

S4. Analysis of the different inversions in previous step S3, focusing on their performance against vertical profiles at FTIR CO stations, as well as in situ observations from surface networks (e.g. GMD, GAW). Determination of the best set of emissions and OH fields – although the differences between different solutions might be possibly small in comparison with uncertainties related to other parameters. Sensitivity studies exploring the effects of alternative a priori emissions, emission set-ups, vertical mixing parameterizations might additionally be conducted to assess these effects.

The main output of this study will therefore be:

(1) an updated top-down determination of CO emissions and photochemical productions, based on a wide range of available literature constraints

(2) an assessment of the sensitivity of the top-down emissions to errors in [OH] as well as other model parameters

(3) a determination of the added value represented by vertical CO profiles at FTIR stations

3.2.4 Current results

The step S1 (see above) has been completed, i.e. a 4-dimensional OH field ($[OH]_{MCF}$) consistent with the MCF constraints has been derived with the IMAGES model. Without the constraint, the average [OH] in the Northern Hemisphere would be significantly larger than in the Southern Hemisphere (by a ratio of ~1.4). An alternative OH distribution, also consistent with MCF, but with a different seasonality and intrahemispheric distribution, is provided by the climatology from Spivakovsky et al. (2000) downscaled by a factor of 0.92, hereafter denoted $[OH]_{S92}$ (Patra et al., 2014). The relevance of the OH adjustment for CO (inverse) modelling is clear from the comparison of the model calculations with CO total columns from the MOPITT (Measurements of Pollution in the Troposphere) version 5

(Deeter et al., 2013), as seen on Figure 2.1. The lower OH concentrations in the Northern Hemisphere lead to a better agreement of the model with observed CO columns.

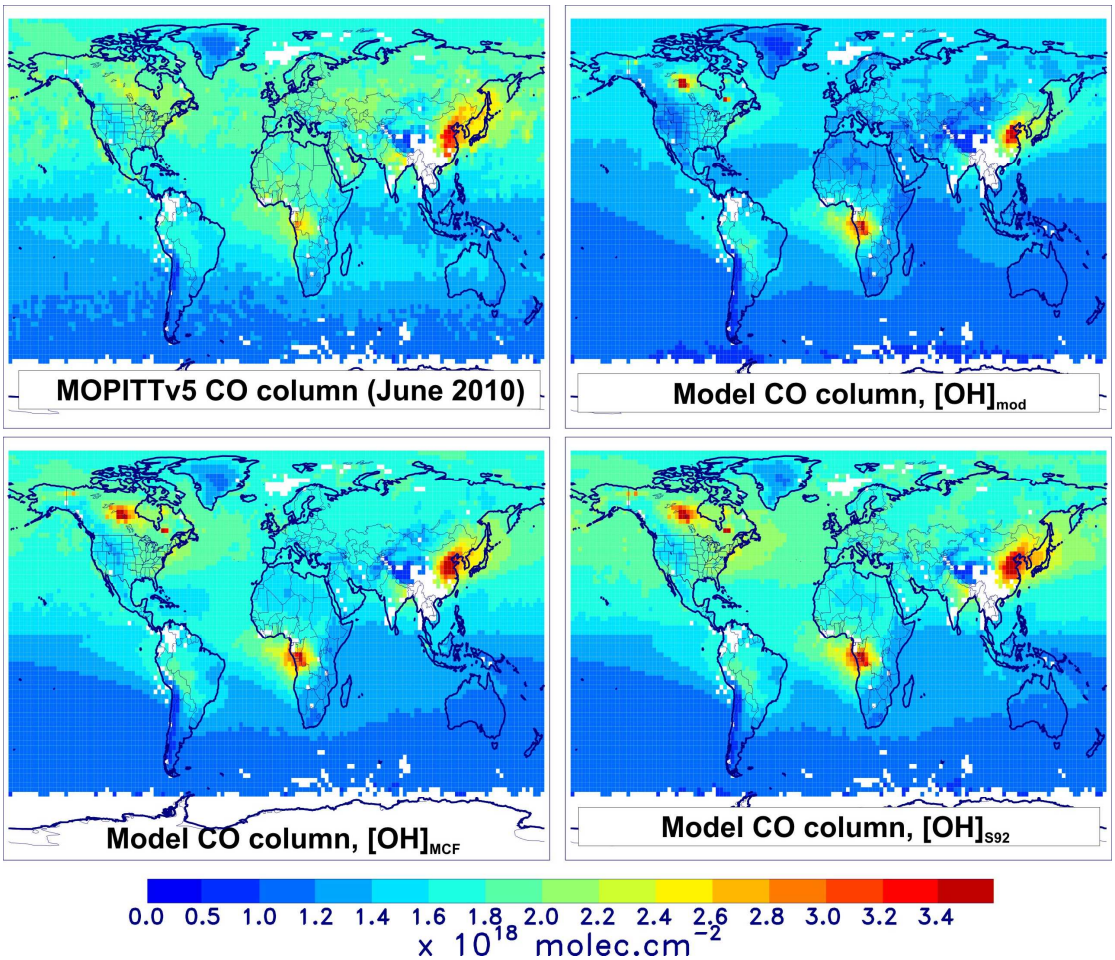

Figure 2.1. Monthly averaged CO total column (1018 molec. cm-2) for June 2010, retrieved from MOPITTv5 and model-calculated using IMAGES with different OH fields.

3.2.5 Conclusions so far and outlook

The uncertainty in the hemispherically averaged [OH] is estimated at about 18% based on estimated uncertainties on global OH and on the interhemispheric ratio (12% each). We define the following source inversions to be conducted in the coming months:

(1) STD using $[OH]_{MCF}$,

(2-3) MCF_HIGH and MCF_LOW using $[OH]_{MCF}$ increased or decreased by 18%, respectively,

(4) SPIV with $[OH]_{S92}$,

(5-6) SPIV_HIGH and SPIV_LOW, using $[OH]_{S92}$ increased or decreased by 18%, respectively.

In this way, the variability in the hemispheric OH averages and the variability in the intrahemispheric distribution and seasonality are explored. The CO sources will be optimized using MOPITT data (Step S3) and the optimized CO fields will be evaluated against ground-based data (S4), in particular the vertical CO profiles from FTIR stations. This will then allow

us to determine the potential added values of vertical profiles for constraining the CO budget.

3.3 Aerosols (FMI)

3.3.1 Scope of the assessment

Atmospheric aerosol particles remain the largest source of uncertainty in the estimates of current drivers of climate change (IPCC, 2013). A better estimate of global aerosol fields both in polluted and pristine environments is therefore an urgent research topic. Given the short lifetime of atmospheric aerosols (from hours to ~1 week in the troposphere) and the relatively sparse temporal resolution of satellite-based observations (pass over a specific site every 0.5-16 days depending on the instrument), it is likely that satellites miss out on some aspects of the atmospheric aerosol variability. Further limitations of most satellite instruments are that they can observe aerosols only in cloud-free conditions, there are no observations during nighttime, and information on aerosol composition is very limited. On the other hand, the surface-based Aerosol Robotic Network (AERONET) (Holben et al., 1998) provides long-term, continuous measurements of Aerosol Optical Depth (AOD) and other aerosol optical and radiative properties from dozens of (mostly continental) measurement sites. These continuous measurements enable a good characterization of local aerosol variability; however reasonable geographical coverage is obtained only over parts of Europe and the US, and elsewhere long-term AERONET measurements are very scarce. Given these respective limitations of both satellite and surface-based observations, it is important to identify the geographical regions that currently suffer from poor observational constraints of aerosol properties in order to guide the development of future observational capabilities.

As such, in order to overcome this issue, the use of a global aerosol-climate model was proposed in order to identify the geographical gaps in the surface-based and sub-orbital observing capabilities of atmospheric aerosols and to pinpoint the regions where additional surface-based measurements would best fill gaps in current observational capabilities.

3.3.2 Model used and planned simulations

In this study, the development version of the global aerosol-climate model ECHAM-HAMMOZ (ECHAM6.1-HAM2.2-SALSA) was used (Stier et al., 2005; Bergman et al., 2012]. The model consists of an atmospheric core model ECHAM, which is used to solve the fundamental equations for the atmospheric flow and physics and tracer transport, and of an aerosol model, HAM. Sectional Aerosol module for Large Scale Applications (SALSA) was implemented to calculate aerosol microphysics (Bergman et al., 2012]. SALSA uses 10 size sections to cover the aerosol size range from 3 nm to 10 µm. Anthropogenic and biomass burning aerosol emissions were described with AeroCom-II Atmospheric Chemistry and Climate Model Intercomparison Project (ACCMIP) data (Riahi et al., 2007, 2011] and provided as monthly average emission fields. Biogenic emissions were simulated with an interactive biogenic emission model MEGAN, which determines emissions of terpenes and isoprenes as a function of temperature, available solar radiation, soil moisture, and carbon dioxide concentrations. To account for atmospheric SOA formation, a scheme based on the

volatility basis set (VBS) (Donahue et al., 2011) was introduced into the model. It enables the modelling of the condensation and evaporation of semi-volatile organic compounds (sVOC) correctly. The Global Fire Emissions Database (GFED3) was implemented to account for the biomass burning emissions. The modeled AOD is calculated at 550nm using concentrations of dust and sea salt particles, biomass burning products (black carbon and organic carbon) and anthropogenic aerosols (sulphates, nitrates etc.).

In this study the model was run using a T63 horizontal resolution (roughly 1.9 × 1.9°) and 31 pressure levels that reached up to 10 hPa. The model was nudged using ECMWF reanalysis data to ensure compatibility between the model and the observed atmospheric conditions. The simulation period was 2005-2010 with a three-month spin-up. The model produces three-hourly average output.

3.3.3 Planned analysis

Satellites, even with a near constant sampling frequency for a given grid box, are neither intended nor able to provide a representative diurnal variability of AOD. As such, ground based measurements ought to be used instead. As Arola et al (2013) showed based on AERONET measurements, the site-specific diurnal AOD pattern varies significantly due to several potential reasons (meteorology, proximity to pollution sources, transport etc). The specific objective of this study was to investigate whether the global aerosol-climate model ECHAM-HAMMOZ has the capacity to reproduce these diurnal cycles and if so, could it be used to indicate in which other regions (that do not have AERONET coverage) such cycles could be found.

3.3.4 Current results

The model performance was assessed by comparing the measured and modelled AOD diurnal variation at 108 AERONET locations around the world. The stations were chosen based on a requirement of a minimum of 100 days of data available, each day having at least one observation both before and after the local solar noon. The AERONET level 2.0 direct sun data of AOD at 500 nm (from 5:00 to 17:00) were used as input to form the diurnal patterns during the summer season covering several years, depending on the location.

All the individual summer AOD observations were used to calculate the departures form the daily mean. Each hourly departure was then averaged for each hour of the local time to form the average daily cycle of the departures at each site. The relative departure was then calculated by dividing each hourly-mean absolute departure by the overall summer AOD mean. In the process of model validation, the 3-hourly average was used to facilitate the comparison to the model output.

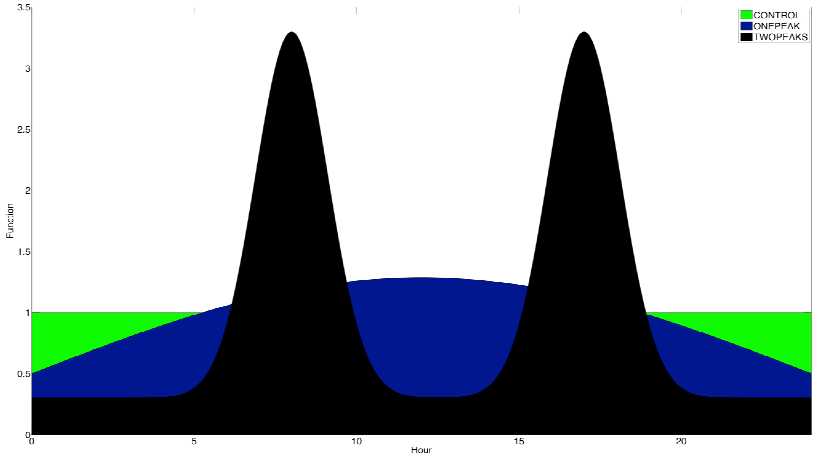

Figure 3.1. The diurnal cycle functions used for the CONTROL (green), ONEPEAK (blue) and the sensitivity analysis TWOPEAKS (black).

ECHAM was run with three configurations for the anthropogenic aerosol emissions:

1. CONTROL – with all the above schemes intact and constant monthly anthropogenic aerosol emission.
2. ONEPEAK – as the CONTROL run, but an artificial diurnal cycle for the anthropogenic emissions was introduced to the model by using a cosine function that peaks during midday. The amplitude of the cosine function was chosen so that the night time minimum was half of the normally constant emissions flux and daytime maximum was roughly 30% more. Additionally, the cosine function was made to preserve the daily total emission flux (Figure 3.1).
3. TWOPEAKS – as the CONTROL run, but with an exaggerated diurnal variation of the anthropogenic aerosol emissions peaking at 8 AM and 5 PM (in the form of a sum of two exponentials), used for sensitivity analysis. In this case the night -time minimum was chosen to be 30% of the normally constant emissions flux while the daytime maxima were about 10 times higher than the minimum. As in the previous case, the exponential function was made to preserve the daily total emission flux (Figure 3.1).

When comparing the model CONTROL and ONEPEAK runs to the observations, only 3 of 108 locations investigated were found to be consistent with the observed AOD diurnal variations in terms of both magnitude and pattern (one example in Figure 3.2a). For the rest of the stations, modelling estimates of the variability shows considerable deficiencies with regard to the daily profile (Figure 3.2b). The inclusion of a cosine daily variability in the modelled anthropogenic emissions (the ONEPEAK run) does not influence the model output in any significant way. Both the daily trend and the magnitude discrepancies remain at the same level as in the CONTROL run.

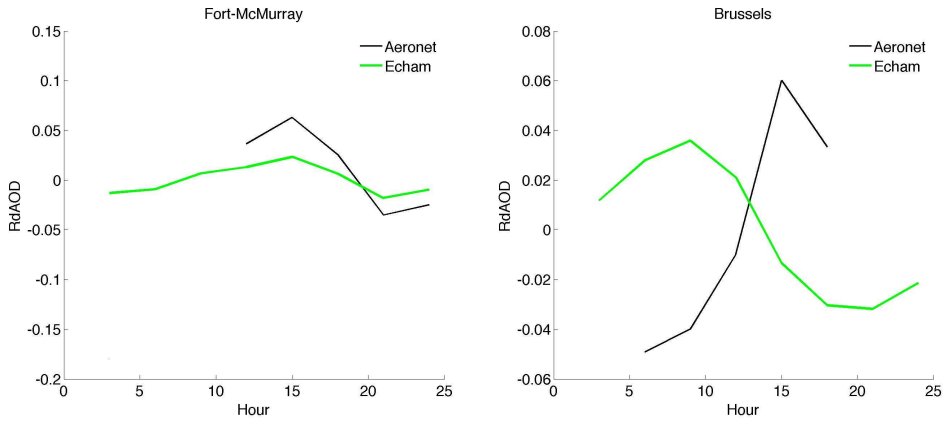

Figure 3.2. Simulated and measured diurnal variability of relative AOD departures from the daily mean. Fort McMurry is one of the three locations where the model agrees well with the measured AOD, while Brussels is a typical example of model-observations mismatch. a) CONTROL run. b) ONEPEAK run.

As the cosine function introduces a weak variation of the anthropogenic emissions with no conclusive effects on the AOD diurnal variation, a stronger function in the form of a sum of two exponentials was considered as a simplistic method of estimating the sensitivity of the modelled AOD output to the variation of the anthropogenic emission input. Figure 3.3 presents the effect of the exponential function at the same two locations as in Figure 3.2. The first evident conclusion is that the model is weakly sensitive to the strong artificial diurnal cycle introduced in the TWOPEAKS run. Its effect is mostly observed at the extremes of the AOD relative departure, that is the minima/maxima are in general affected more than the intermediate AOD values. The architecture of the AOD diurnal cycles remains basically analogous to that obtained in the CONTROL and ONEPEAK runs.

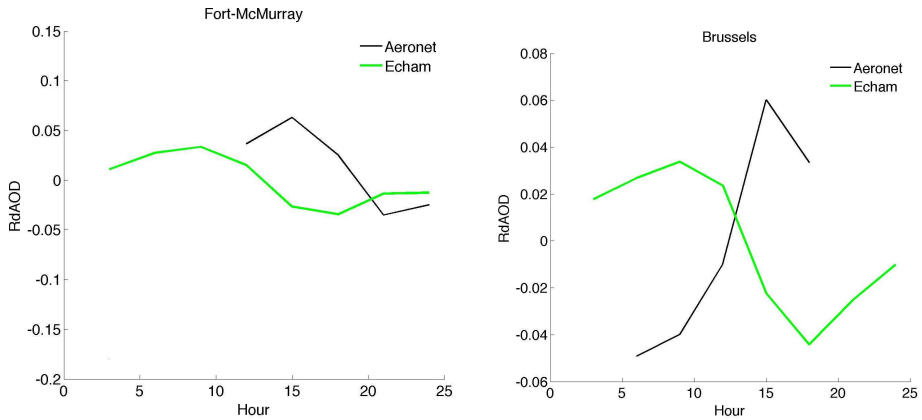

Figure 3.3. As in Figure 3.2, but TWOPEAKS run.

The daily trend analysis is illustrated in Figure 3.4, where the comparison between the observations and the three model runs is presented. The model reproduces the AERONET AOD relative departure within a factor of 2 in less than 20% of the cases. It also indicates that all three simulations are in general unable to reproduce the daily maxima/minima.

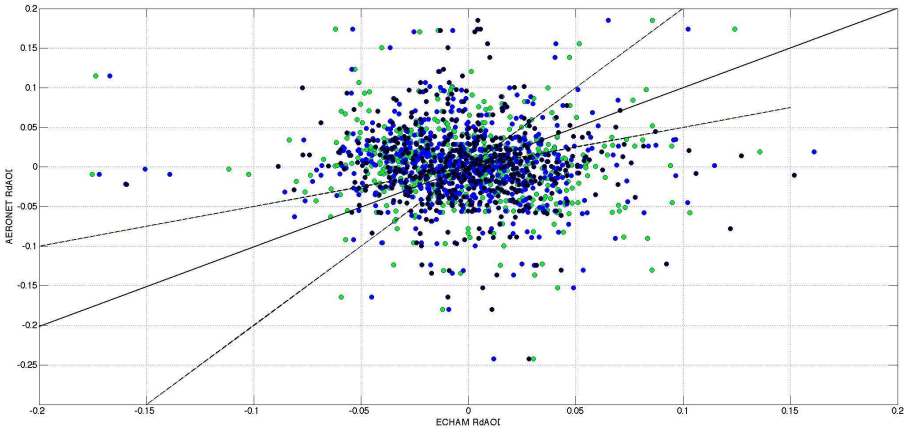

Figure 3.4. Scatter plot of the observed (AERONET) and simulated AOD relative departures. The model is sampled in the same temporal and spatial location as of the observations. The green dots represent the CONTROL run, the blue dots the ONEPEAK run and the black dots the TWOPEAKS run. The 1:1 continuous line is included for clarity.

3.3.5 Conclusions and future activities

Within GAIA-CLIM, FMI have performed global aerosol-climate model simulations in order to identify geographical gaps in the surface-based observing capabilities of atmospheric aerosols. The studied ECV was aerosol optical depth (AOD). Our simulations aimed at characterizing how representative the AERONET stations are of their respective environments in terms of aerosol variability. The chosen approach relied on the assumption that the ECHAM-HAMMOZ model is capable of capturing the qualitative features of atmospheric aerosol variability, and thus can be used to identify gaps in current observation systems in terms of geographical coverage. However, the detailed comparison of the modelled and the observed aerosol variability at 108 selected AERONET sites in different environments shows that, unfortunately, the model is not equipped to handle this specific issue. Implications and possible remediation will be explored.

3.4 Ozone and related trace gases (KIT)

3.4.1 Scope of the assessment

The evolution of the stratospheric ozone layer over the 21st century will be controlled by the decreasing concentration of ozone depleting substances (ODS) following the Montreal Protocol and its amendments, as well as by climate change due to the increase of greenhouse gases. Tropospheric ozone, itself a greenhouse gas, will also be influenced by changes in precursor emissions and indirectly by climate change due to the increase of greenhouse gas concentrations. One sensitive region is the tropics, where chemistry climate models predict that stratospheric ozone will not recover following the reduction of ODS, but will further decrease due to changes in large scale circulation (enhancement of the Brewer-

Dobson circulation) as a result of increased concentrations of greenhouse gases. However, a clear attribution of past changes in tropical column ozone is complicated by uncertainties in concurrent increases in tropospheric ozone.

Here we will assess gaps in the geographical coverage of ozone column measurements (– as well as gaps in relevant parameters), and in particular we will assess whether the coverage of existing networks is sufficiently representative to detect expected climate change signals. Results so far focus on ozone column observations in the tropics since the existing coverage in this region is particularly sparse.

3.4.2 Model system and simulations used

The data for our analysis are part of a Chemistry–Climate Model Initiative (CCMI) recommended set of simulations by the Earth System Chemistry Integrated Modelling (ESCiMo) consortium. The ESCiMo simulations have been performed at DKRZ in Hamburg using version 2.51 of the ECHAM/MESSy Atmospheric Chemistry (EMAC) model. The long-term simulation comprises a time span of 150 years starting in 1950 and combines hindcast and projections. The future greenhouse gas emissions are based on the RCP6.0 scenario, while the sea surface temperatures and sea ice cover are taken from HadGEM2 simulations. The ozone data are available as monthly averages in a spatial resolution of T42L47 (approx. 2.8°x2.8° and with a top level 1 Pa). For further detailed information, we refer to the corresponding publication by Jöckel et al. 2016.

3.4.3 Planned analysis

In Fig. 4.1, the presently active NDACC measurement stations are shown on a global map. The colour code used indicates zonal bands. While the majority of stations are located in mid-latitude Europe (green), less than ten stations are based in the tropics (red) and only one in the northern hemisphere subtropics (golden, Izaña, Tenerife, Spain). Of the tropical stations only two are in the deep tropics close to the equator (Paramaribo, Suriname and Natal, Brasil). Given this sparseness of stations in the deep tropics, we are going to investigate how representative those available data are in terms of zonal and global ozone trends.

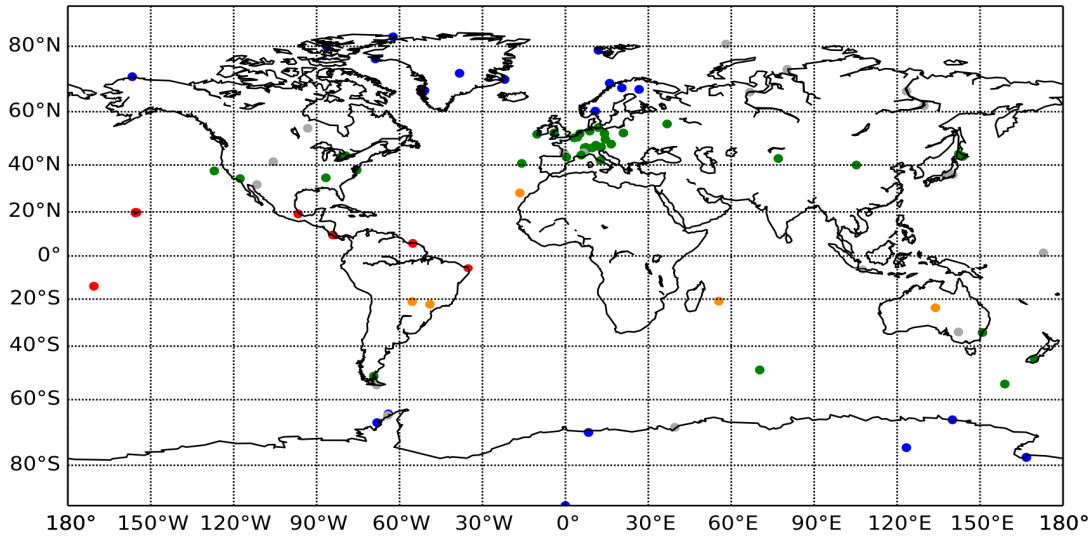

Figure 4.1. NDACC measurement stations. The colour coding indicates the zonal band: Red: tropics (20° N – 20° S), golden: subtropics (20°-30° N/S), green: mid-latitude (30°-60° N/S), blue: high-latitude (60°-90° N/S); grey: presently inactive stations. See http://www.ndsc.ncep.noaa.gov.

From the 150 years of ESCiMo simulation, the total column ozone has been used. For eight tropical stations, we have evaluated data at the nearest model grid point with respect to the real location in both the horizontal and vertical position. A moving average with a time window of seven years has been used to smooth periodical ozone variation (e.g. seasons). The eleven years solar cycle remains as an underlying periodical signal.

3.4.4 Current results

In various climate simulation studies, the tropical upwelling has been found to be increasing by the end of the 21st century. As a consequence of the accelerated Brewer Dobson Circulation (BDC) there is very likely to be a decrease of tropical lower-stratosphere ozone. Beside this dominant dynamical affect, a recent study (Meul et al. 2014) identifies subsidiary contributions from changes in chemical ozone production and destruction, which may be expected to introduce altitude-dependent alterations. While the contribution of chlorine to the ozone depletion declines, the importance of HO_x and NO_x rises. Regarding the ozone production, methane photolysis may slightly gain importance, which is noteworthy in case of future scenarios seeing a significant rise in methane emission (RCP8.5). The tropospheric ozone is mainly affected by this increase in methane.

In Fig. 4.2, the resulting ozone column trends are depicted for tropical zonal mean (bold blue line) and eight NDACC stations located in the tropics (differently coloured dashed lines). The ozone divergence is shown with respect to the annual mean of 1980. The shaded area represents the standard deviation of the moving average of the tropical zonal mean. In Fig. 4.2a, b, c respectively, the total column, tropospheric column and stratospheric column ozone are displayed.

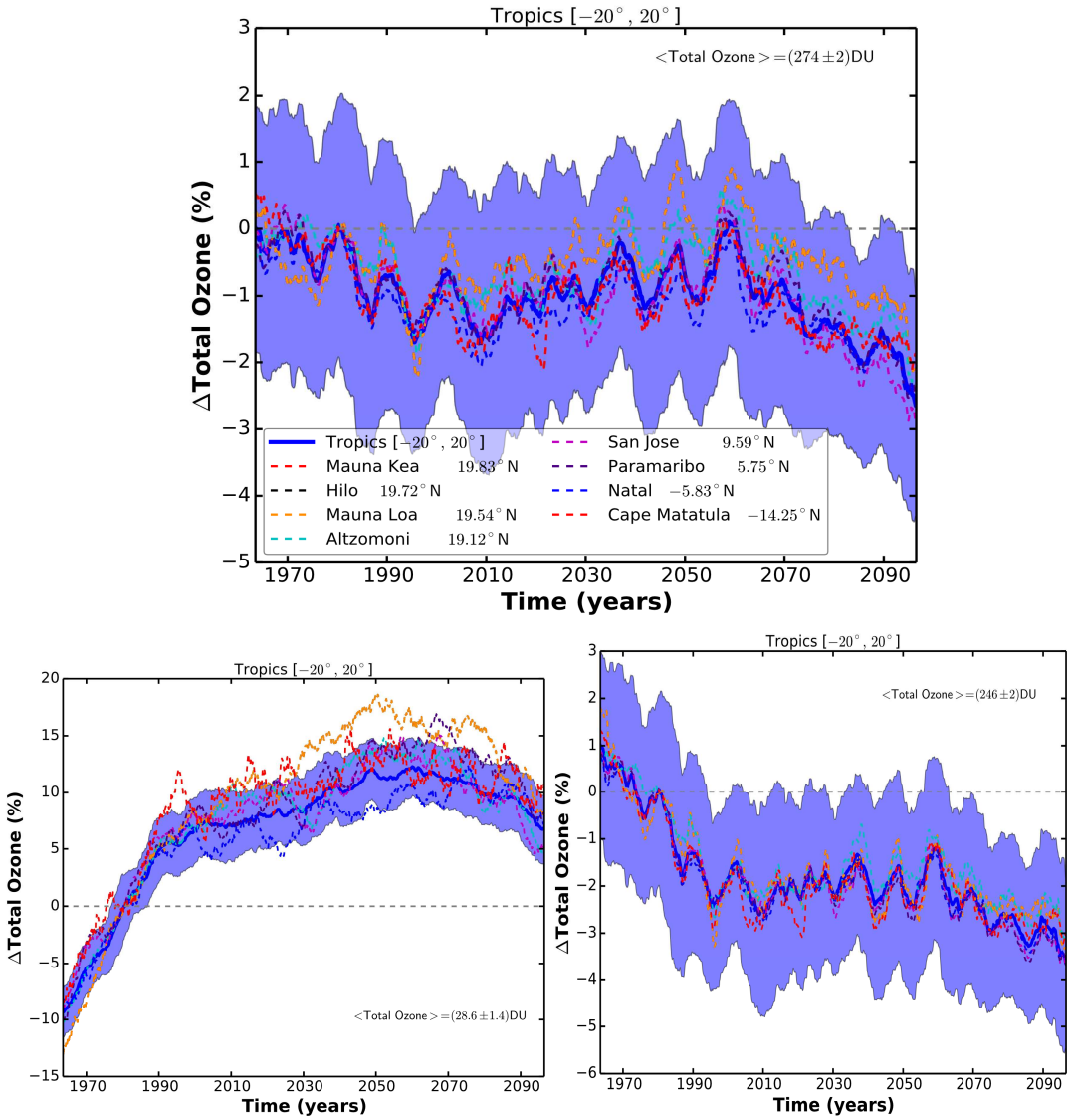

Figure 4.2. Column ozone trends for zonal averages and currently active NDACC stations (the latter as simulated, not as observed). Data are taken from long-term, free-running ESCiMo simulations (RC2-base-05). NDACC station location were provided through the NDACC webpage. The bold, blue line represents the corresponding tropical zonal mean over the period of 150 years. Data have been smoothed using a moving average approach with a window size of seven-years. The remaining underlying periodical signal corresponds to the solar cycle. The blue shaded area represents the standard deviation of the moving average. The change of ozone is with respect to the annual-mean of 1980 in the tropics (a) Total column. (b) Tropospheric column. (c) Stratospheric column.

For the total column ozone (Fig 4.2a), three major periods can be identified:

- Ozone hole (~1979-2010)
- Recovery (~2010-2060)
- Accelerated circulation (~2060-…)

The divergence between individual stations and the true area average varies within 2% over 150 years. Within the ozone hole period, all local ozone columns agree rather well with the

zonal mean. In the recovery period, the northern-most stations at Hawaii (Mauna Kea, Hilo, Mauna Loa), diverge most strongly from the zonal mean. Splitting the total column in troposphere (Fig 4.2b) and stratosphere (Fig 4.2c) fraction, an underlying rise in troposphere ozone in the course of the 21st century can be identified, which is strongest for the northern-most stations. In agreement with other studies, the stratosphere ozone column in the tropics does not see a recovery by mid-century.

3.4.5 Conclusions and future activities

Our results so far indicate that observations from stations such as Paramaribo (Suriname), San Jose (Costa Rica) and Cape Matatula (American Samoa) cover the zonal ozone column trend well. While these few individual stations are generally representative for stratospheric ozone observations in the tropics at large, for tropospheric ozone there are larger discrepancies. Here, we also show that the expected changes in total ozone in the tropics are caused almost equally by changes in stratospheric ozone and by changes in tropospheric ozone. This may have implications for the validation of long-term ozone observations in the tropics. A more thorough statistical analysis has yet to be conducted to fully establish and verify these first results for the tropics as well as other latitude bands.

3.5 Assessing geographical gaps for reference temperature and humidity in-situ data (ECMWF)

3.5.1 Scope of the assessment

Satellite instruments sensitive to atmospheric temperature and humidity are regularly assimilated into Numerical Weather Prediction (NWP) and Re-analysis systems and contribute to the atmospheric (re)analysis products of temperature, humidity and vector wind. Before assimilating a new instrument, the radiances are compared to the re-analysis or NWP first guess fields (forecasts from the previous cycle) in radiance space, in order to assess the quality of the data. The short-range forecasts, also known as the background (B), are transformed into radiance space using a radiative transfer forward model and then compared to the observed radiances (O) for the different instruments. Global statistics of O - B tend to show constant global biases as well as biases that vary geographically or as a function of orbital parameters. In some cases these biases indicate errors in the satellite instrument radiances (e.g. due to calibration) or in the radiative transfer forward model, both of which must be corrected either prior to or during the assimilation, in order to prevent these errors from propagating into the reanalysis products and/or the forecasts of NWP systems. In some cases the biases can be easily diagnosed as due to the instrument, such as the orbital-dependent biases found for the SSMI/S instrument (Bell et. al 2008, Geer et. al. 2010). These biases were clearly visible in maps of O - B and diagnosed to be related to solar intrusions into the warm calibration load and emission from the main reflector of the instrument. In other cases it is less obvious whether the biases observed are due to instrument errors or errors either in the radiative transfer model or in the NWP short-range forecasts. Furthermore, while the presence of instrument-related errors can often be

detected, it is difficult to quantify them since the errors in the forecast are not known exactly.

Reference in-situ radiosonde measurements for temperature and humidity with calculated uncertainty values, such as the GRUAN network, have the potential to diagnose the sources of bias observed in O – B statistics, as well as to quantify these biases and give confidence intervals for these values. In work package 4 of the GAIA-CLIM project, a GRUAN processor is being developed which will transform the GRUAN observations and uncertainties into radiance space for different satellite instruments. The GRUAN processor will allow a comparison between the reference in-situ observations and both the NWP model backgrounds and the satellite instrument observations (both in radiance space), and could help in diagnosing and quantifying the biases observed for the different satellite instruments.

However, while the GRUAN data are SI-traceable and have accurate estimates of uncertainties, they are only available for a limited number of locations and it is not clear whether the network is geographically capable of diagnosing the types of bias observed in O – B statistics, in particular biases that vary geographically. In this study we aim to assess the geographical capabilities of the GRUAN network for diagnosing the sources of O – B biases for a number of different satellite instruments.

3.5.2 Methods

In this study we will firstly perform a review of the types of bias observed in O – B values for key satellite instruments, including the AMSU-A and MHS microwave temperature and humidity sounding instruments, and the Chinese FY-3C microwave temperature and humidity sounding instruments, MWTS-2 and MWHS-2, which are being assessed in work package 4 of the GAIA-CLIM project. In order to assess the geographical representiveness of the GRUAN sites, the O – B values for these instruments will then be subsampled at the locations of the GRUAN sites and the biases of the sub-sampled dataset compared to the global O – B statistics. If the statistics for the subsampled dataset are comparable to the global values then this will indicate whether the GRUAN network is 'geographically capable' of diagnosing such biases. This will also allow us to better understand which types of bias the GRUAN data can diagnose as well as areas where we may have geographical gaps. It should be noted, however, that this study focuses on gaps in geographical coverage only and does not include an assessment of potential temporal or spatial mismatch gaps in the GRUAN measurements

3.5.3 Current results

Microwave Temperature and Humidity Sounders

The main microwave temperature sounding instrument to be used in NWP and reanalysis models in recent years is the Advanced Microwave Sounding Unit –A (AMSU-A) instrument. To date, there have been 7 AMSU-A's flown on both American and European satellite platforms, 6 of which are still currently operational. In addition the Advanced Technology

Microwave Sounder (ATMS) instruments, flown on the American Suomi-NPP satellite, have the same channels, as does the Chinese MicroWave Temperature Sounder -2 (MWTS-2) instrument, flown on the FY-3C satellite. Conical scanners such as the Special Sensor Microwave Imager/Sounder (SSMI/S) also have these channels, but in this study we will focus on the cross-track scanning instruments of AMSU-A, ATMS and MWTS-2. The temperature sounding channels of these instruments each measure in the frequency range 50 – 60 GHz, sampling in between oxygen absorption lines, and are each sensitive to temperature at different atmospheric heights. The channel numbers and frequencies are given in Table 5.1. The sensitivity of each channel to different atmospheric heights can be illustrated by the Jacobians given in Fig. 5.1. As this figure shows, each channel is sensitive to temperature over a range of heights, with a peak height sensitivity. In this study we will exclude the channels that peak above the maximum height of GRUAN radiosondes (approximately 5 – 10 hPa), which means excluding channels 12 – 14.

Microwave Humidity Sounders measure around the water vapour absorption line at 183 GHz. These sounders include the MHS (Microwave Humidity Sounder) instruments, ATMS and the MicroWave Humidity Sounder -2 instrument flown on FY-3C (all of which are cross-track scanning instruments). There are currently 4 MHS instruments flown on 2 NOAA satellites and 2 MetOp satellites, one ATMS and one MWHS-2. The MHS instruments have 3 sounding channels around 183 GHz. The ATMS and MWHS-2 instruments have the same channels and an additional two channels. The channel numbers and frequencies of MHS, MWHS-2 and ATMS are given in Table 5.2. Each sounding channel on these instruments is sensitive to relative humidity at different heights of the atmosphere. The sensitivity to different heights can be illustrated by the humidity Jacobians, shown in Fig. 5.2 for the MWHS-2 channels. It is worth noting that the Jacobians themselves vary with atmospheric humidity so that in a dry atmosphere the channels peak at lower heights and in a wetter atmosphere they peak higher up. This is different to the AMSU-A temperature sounding channels, since the AMSU-A is sensitive to oxygen which is a well-mixed gas.

Table 5.1. Temperature Sounding channel numbers and frequencies for the AMSU-A, ATMS and MWTS-2 instruments

Channel frequency (GHz)	AMSU-A channel number	ATMS channel number	MWTS-2 channel number
53.596 ± 0.115	5	6	3
54.4	6	7	4
54.94	7	8	5
55.5	8	9	6
57.29	9	10	7
57.29 ± 0.3222 ± 0.217	10	11	8
57.29 ± 0.3222 ± 0.048	11	12	9
57.29 ± 0.3222 ± 0.022	12	13	10
57.29 ± 0.3222 ± 0.010	13	14	11
57.29 ± 0.3222 ± 0.0045	14	15	12

Table 5.2. Humidity Sounding channel numbers and frequencies for the MHS, ATMS and MWHS-2 instruments

Channel frequency (GHz)	MHS channel number	ATMS channel number	MWHS-2 channel number
183.31 ± 1.0	3	22	11
183.31 ± 1.8	-	21	12
183.31 ± 3.0	4	20	13
183.31 ± 4.5	-	19	14
183.31 ± 7.0 (ATMS/MWHS-2)/ 190.311(MHS)	5	18	15

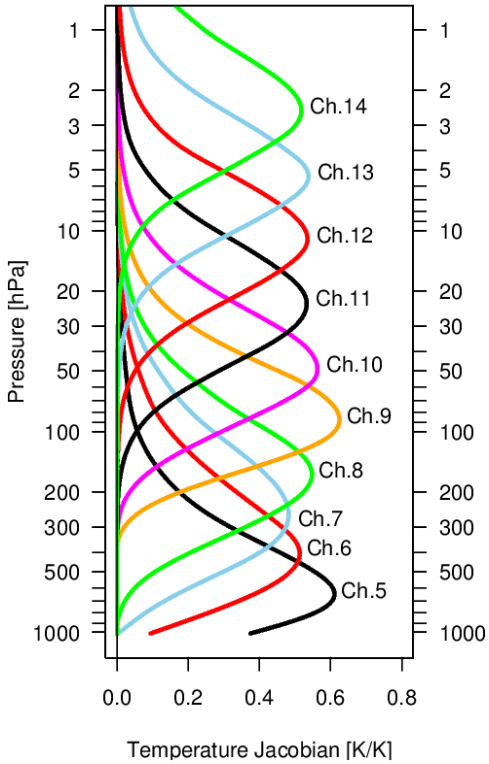

Figure 5.1. Temperature Jacobians for AMSU-A sounding channels (normalised by the change in ln pressure of each model level).

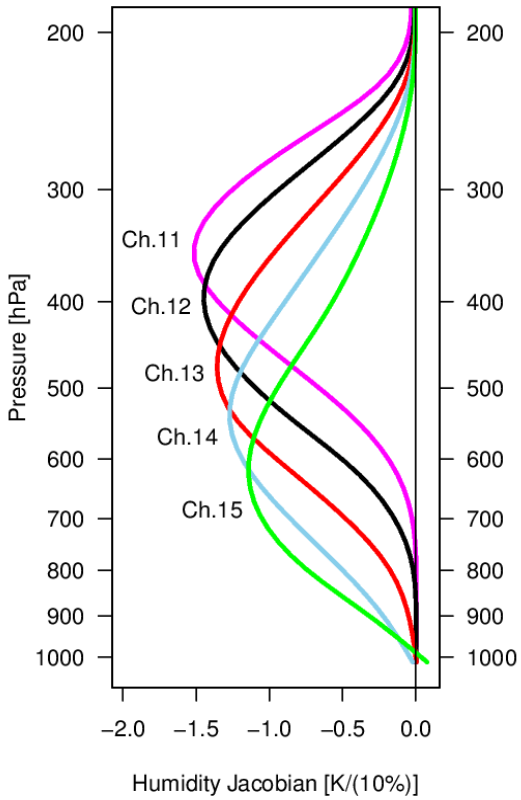

Figure 5.2. Humidity Jacobians for the MWHS-2 183 GHz humidity sounding channels (normalised by the change in ln pressure of each model level).

Biases in O – B statistics

The types of bias typically observed for the O – B values of microwave temperature and humidity sounding instruments include:

- Globally constant biases
- Airmass-dependent biases
- Scan-angle dependent biases
- Scene-temperature dependent biases

Examples of these biases are shown in Figs. 5.3 – 5.5. The background values from these plots were calculated from the ECMWF short-range temperature and humidity forecasts, and transformed into radiance space using either the clear-sky radiative transfer model RTTOV (for AMSU-A, MWTS-2 and ATMS) or the all-sky radiative transfer forward model RTTOV-SCATT (MWHS-2 and MHS). All data were screened for cloud and averaged over 1 month for June 2014.

Figure 5.3 shows the airmass-dependent biases observed in channel 8 of MetOp-B AMSU-A. Similar biases can be observed for this channel for most AMSU-A instruments, and this bias has recently been hypothesized to be due to on-orbit shifts in the frequency pass-bands for these instruments (Lu and Bell 2010). GRUAN data could potentially help to either confirm this hypothesis or indicate that some or all of these biases are due to the model background. The locations of the GRUAN sites are also shown in Figure 5.3. Note that there are sites which are currently certified to GRUAN standards, sites awaiting certification and sites which are currently inactive (see www.dwd.de/EN/research/international_programme/gruan/home.html for more information). An initial look at the GRUAN sites plotted on this map indicates that if all three types of site are included they are geographically capable of observing this type of bias, since the bias appears to vary with latitude and there are GRUAN sites for a range of latitudes. Taking account of only the certified sites, however, indicates a gap in the tropics and in the south polar region (latitudes south of 60°S). It is therefore important to fill this gap with the certification of Davis in Antarctica, and the potential GRUAN sites in the tropics (La Reunion, Singapore, Melbourne, Alice Springs and Darwin).

Figure 5.4 shows the global biases observed for the MWTS-2 instrument, which are consistently negative (Lu et al 2015), contrary to the same channels on other satellite instruments. Given that the biases of the same channels of AMSU-A are much smaller it is thought that these strong biases are due to the MWTS-2 instrument.

Figure 5.5 shows scan angle biases which are remarkably similar for the same channels on different instruments. This bias is therefore likely to be due to radiative transfer model error or NWP background model error.

In this study we will sub-sample O – B statistics at GRUAN sites and see if they show the same biases as for the global data sample, presented in Figs. 5.3 – 5.5.

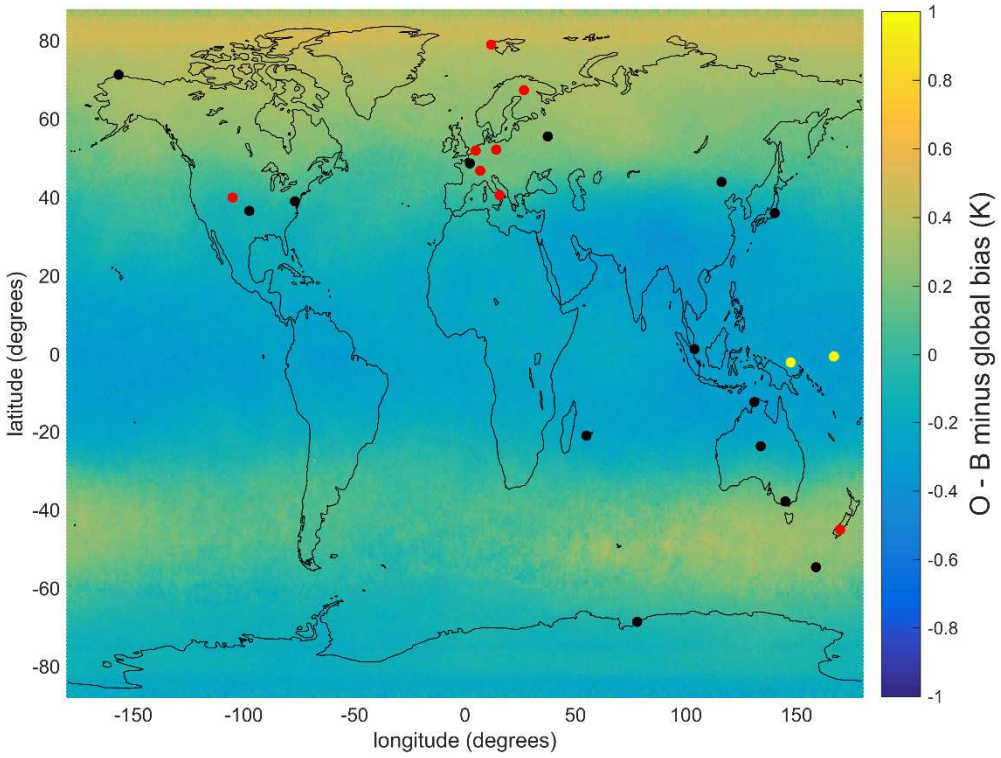

Figure 5.3. Map of the Mean observation minus ECMWF background, averaged over 1 month (July 2014), for MetOp-B AMSU-A channel 8. The global bias has been removed from the data, such that the values are centred around zero. The locations of the GRUAN stations are also shown, as dots, with red dots indicating certified stations, black dots the stations that are currently uncertified and yellow dots the inactive stations.

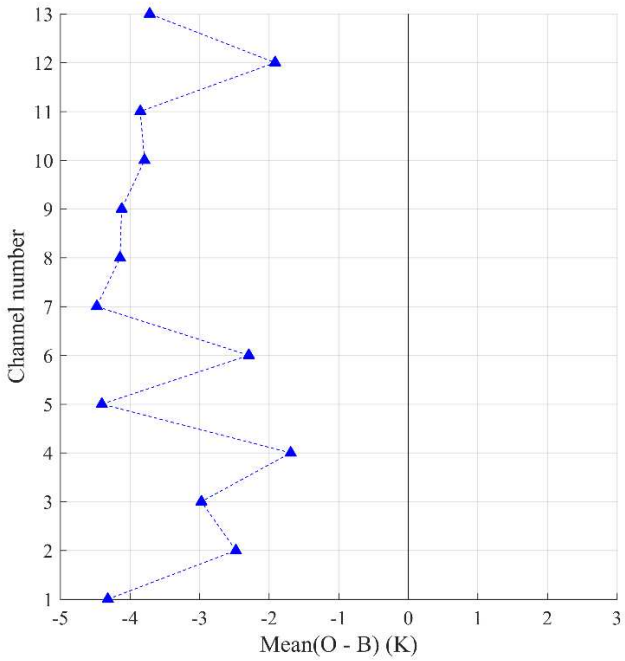

Figure 5.4. Global biases as a function of channel number for the MicroWave Temperature Sounder -2 (MWTS-2) instrument flown on the FY-3C satellite.

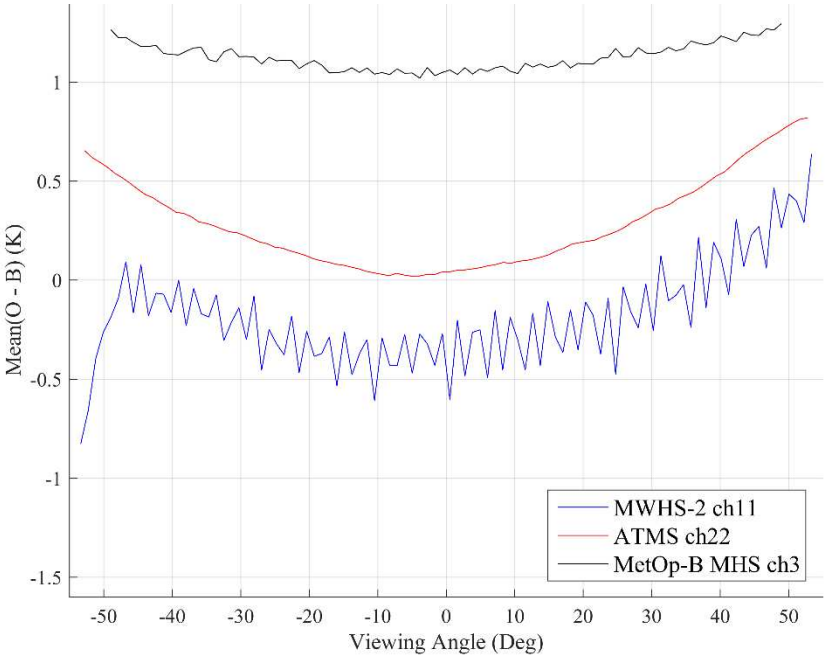

Figure 5.5. Scan-angle biases for the 183.31 +/- 1.0 GHz channels on 3 different satellite instruments, including FY-3C MWHS-2 (channel 11), Suomi-NPP ATMS (channel 22) and MetOp-B MHS (channel 3).

3.5.4 Conclusions and future activities

This study has only recently begun and therefore the work is ongoing. An initial look at maps of the airmass-dependent biases for MetOp-B AMSU-A channel 8 indicate that the current GRUAN sites have a gap in the tropics and over the south pole, which would make them unable to identify the source of this type of bias. However a number of radiosonde sites are awaiting GRUAN certification and if these sites are certified then the GRUAN network could be capable of identifying such biases. Key sites awaiting certification appear to be those in tropics (La Reunion, Singapore, Darwin, Alice Springs) and the site in Antarctica (Davis) which would be the only site to sample the region below 60°S.

Future work in this study will extend the assessment of airmass-dependent biases to other channels on AMSU-A and to the humidity instruments, and also investigate whether the GRUAN sites are capable of identifying the sources of global biases and satellite scan-angle dependent biases.

4. Overall conclusions and recommendations

In this report we have highlighted a range of modelling studies and approaches that show potential to help inform observational network design practices.

The ECVs and gaps covered by the model-based gap analysis are summarized in Table 4. Clearly, most of the analysis focuses on the spatiotemporal aspects, as these are the scales that can be directly assessed with models. None of the analyses address the technical, governance, or uncertainty-related gaps.

Table 4: A summary of the gap analysis presented in this deliverable, with respect to the gap types and the ECVs from Section 3. Here the spatiotemporal gap is separated into the spatial and temporal components.

	Spatial coverage	Temporal coverage	Vertical resolution	Uncertainty (per observation)	Uncertainty (wrt. comparator measures, representativeness)	Technical (formats, etc.)	Governance (harmonisation procedures, etc.)	Parameter (need for auxiliary information/parameters)
CO_2	■				■			
CH_4					■			
CO	■	■	■					
AOD	■	■						
O_3	■		■					■
Temperature	■							
Humidity	■							

Given this focus on the spatiotemporal context, it is clear that this is where the most guidance regarding shortcomings in the current ground-based observing systems can be provided. With this in mind, the work in this task over the next period will aim to define regions in which the capabilities to validate spaceborne measurements can be optimally expanded. It will be interesting to see if common regions will emerge across ECVs, which could point to the need for a general expansion of ground-based observation systems to specific regions.

With respect to the four questions raised in Section 2, the work to this point focuses on answering the first three: how best to use models for interpolation and analysis of sparse in-situ measurements; where additional measurements would add the most interpretive value; and the importance of measurement frequency, scheduling and quality. What has not yet been explored is the benefit of fewer measurements with lower uncertainties vs. more measurements with higher uncertainties. This points to an aspect of the analysis that could be expanded upon during the coming year.

5. References

Agustí-Panareda, A., Massart, S., Chevallier, F., Boussetta, S., Balsamo, G., Beljaars, A., Ciais, P., Deutscher, N. M., Engelen, R., Jones, L., Kivi, R., Paris, J.-D., Peuch, V.-H., Sherlock, V., Vermeulen, A. T., Wennberg, P. O., and Wunch, D.: Forecasting global atmospheric CO_2, Atmos. Chem. Phys., 14, 11959-11983, doi:10.5194/acp-14-11959-2014, 2014.

Arola, A., Eck, T.F., Huttunen, J., Lehtinen, K.E.J., Lindfors, A.V., Myhre, G., Smirnov, A., Tripathi, S.N., Yu, H.: Influence of observed diurnal cycles of aerosol optical depth on aerosol direct radiative effect, Atmos. Chem. Phys., 13, 7895-7901, 2013.

Bauwens, M., Stavrakou, T., Müller, J.-F., De Smedt, I., Van Roozendael, M., van der Werf,, G. R., Wiedinmyer, C., Kaiser, J., Sindelarova, K., and Guenther, A.: Nine years of global hydrocarbon emissions based on source inversion of OMI formaldehyde observations, *Atmos. Chem. Phys. Discuss*., doi:10.5194/acp-2016-221, 2016.

Bell W, Candy B, Atkinson N, Hilton F, Baker N, Bormann N, Kelly G, Kazumori M, Campbell W, Swadley S. 2008. The assimilation of SSMIS radiances in numerical weather prediction models. *IEEE Trans. Geoscience. Rem. Sensing*. 46: 884 – 900.

Bergman, T., Kerminen, V.-M., Korhonen, H., Lehtinen, K. J., Makkonen, R., Arola, A., Mielonen, T., Romakkaniemi, S., Kulmala, M., and Kokkola, H.: Evaluation of the sectional aerosol microphysics module SALSA implementation in ECHAM5-HAM aerosol-climate model, Geosci. Model Dev., 5, 845–868, 2012.

Bousquet, P., D. A. Hauglustaine, P. Peylin, C. Carouge, and P. Ciais, Two decades of OH variability as inferred by an inversion of atmospheric transport and chemistry of methyl chloroform, Atmos. Chem. Phys., 5, 2635-2656, 2005.

Deeter, M. N., Martínez-Alonso, S., Edwards, D. P., Emmons, L. K., Gille, J. C., Worden, H. M., Sweeney, C., Pittman, J. V., Daube, B. C., and Wofsy, S. C.: The MOPITT Version 6 product: algorithm enhancements and validation, Atmos. Meas. Tech., 7, 3623-3632, doi:10.5194/amt-7-3623-2014, 2014.

Donahue, N. M., Epstein, S. A., Pandis, S. N., and Robinson, A. L.: A two-dimensional volatility basis set: 1. organic-aerosol mixing thermodynamics, Atmos. Chem. Phys., 11, 3303-3318, 2011.

Geer A, Bauer P, Bormann N. 2010. Solar biases in microwave imager observations assimilated at ECMWF. *IEEE Trans. Geoscience. Rem. Sensing*. 48: 2660–2669.

George, M., Clerbaux, C., Bouarar, I., Coheur, P.-F., Deeter, M. N., Edwards, D. P., Francis, G., Gille, J. C., Hadji-Lazaro, J., Hurtmans, D., Inness, A., Mao, D., and Worden, H. M.: An examination of the long-term CO records from MOPITT and IASI: comparison of retrieval methodology, Atmos. Meas. Tech., 8, 4313-4328, doi:10.5194/amt-8-4313-2015, 2015.

Giglio, L., Randerson, J. T., and Werf, G. R.: Analysis of daily, monthly, and annual burned area using the fourth-generation global fire emissions database (GFED4), J. Geophys. Res., 118(1), 317–328, doi:10.1002/jgrg.20042, 2013.

Guenther, A. B., Jiang, X., Heald, C. L., Sakulyanontvittay a, T., Duhl, T., Emmons, L. K., and Wang, X.: The Model of Emissions of Gases and Aerosols from Nature version 2.1 (MEGAN2.1): an extended and updated framework for modelling biogenic emissions, Geosci. Model Dev., 5, 1471–1492, doi:10.5194/gmd-5-1471-2012, 2012.

Guerlet, S., Butz, A., Schepers, D., Basu, S., Hasekamp, O. P., Kuze, A., Yokota, T., Blavier, J.-F., Deutscher, N. M., Griffith, D. W. T., Hase, F., Kyro, E., Morino, I., Sherlock, V., Sussmann, R., Galli, A., and Aben, I.: Impact of aerosol and thin cirrus on retrieving and validating XCO_2 from GOSAT shortwave infrared measurements, J. Geophys. Res. Atmos., 118, 4887–4905, doi:10.1002/jgrd.50332, 2013.

Holben, B. N., Eck, T. F., Slutsker, I., Tanre, D., Buis, J. P., Setzer, A., Vermote, E., Reagan, J. A., Kaufman, Y. J., Nakajima, T., Lavenu, F., Jankowiak, I., and Smirnov, A.: AERONET – a federated instrument network and data archive for aerosol characterization, Remote Sens. Environ., 66, 1–16, 1998.

IPCC, 2013: Climate Change 2013: The Physical Science Basis. Contribution of Working Group I to the Fifth Assessment Report of the Intergovernmental Panel on Climate Change [Stocker, T.F., D. Qin, G.-K. Plattner, M. Tignor, S.K. Allen, J. Boschung, A. Nauels, Y. Xia, V. Bex and P.M. Midgley (eds.)]. Cambridge University Press, Cambridge, United Kingdom and New York, NY, USA, 1535 pp.

Jiang, Z., Jones, D. B. A., Worden, J., Worden, H. M., Henze, D. K., and Wang, Y. X.: Regional data assimilation of multi-spectral MOPITT observations of CO over North America, Atmos. Chem. Phys., 15, 6801-6814, doi:10.5194/acp-15-6801-2015, 2015.

Jöckel, P.; Tost, H.; Pozzer, A.; Kunze, M.; et al., Earth System Chemistry integrated Modelling (ESCiMo) with the Modular Earth Submodel System (MESSy) version 2.51, Geoscientific Model Development, 9(3), 1153-1200, doi:10.5194/gmd-9-1153-2016, 2016.

Lu Q, Bell W. 2014. Characterizing Channel Center Frequencies in AMSU-A and MSU Microwave Sounding Instruments. *J. Atmos. Ocean. Tech.* 31: 1713-1732.

Lu Q, Lawrence H, Bormann N, English S, Lean K, Atkinson N, Bell W, Carminati F. 2015. An evaluation of FY-3C satellite data quality at ECMWF and the Met Office. *ECMWF Tech. Memo*. 767.

Massart, S., Agusti-Panareda, A., Aben, I., Butz, A., Chevallier, F., Crevoisier, C., Engelen, R., Frankenberg, C., and Hasekamp, O.: Assimilation of atmospheric methane products into the MACC-II system: from SCIAMACHY to TANSO and IASI, Atmos. Chem. Phys., 14, 6139-6158, doi:10.5194/acp-14-6139-2014, 2014.

Meul, S.; Langematz, U.; Oberländer, S.; et al., Chemical contribution to future tropical ozone change in the lower stratosphere, Atmos. Chem. Phys.,14(6) 2959-2971, doi:10.5194/acp-14-2959-2014, 2014.

Müller, J.-F., and T. Stavrakou, Inversion of CO and NOx emissions using the adjoint of the IMAGES model, Atmos. Chem. Phys., 5, 1157-1186, 2005.

Naik, V., A. Voulgarakis, A. M. Fiore, L. W. Horowitz, J.-F. Lamarque, M. Lin, et al. Preindustrial to present-day changes in tropospheric hydroxyl radical and methane lifetime from the Atmospheric Chemistry and Climate Model Intercomparison Project (ACCMIP), Atmos. Chem. Phys., 13, 5277-5298, 2013.

Patra, P. K., M. C. Krol, S. A. Montzka, T. Arnold, E. L. Atlas, B. R. Lintner, B. B. Stephens, et al. Observational evidence for interhemispheric hydroxyl-radical parity, Nature 513, 219-223, 2014.

Riahi K, Gruebler A, Nakicenovic N: Scenarios of long-term socio-economic and environmental development under climate stabilization. Technol Forecast Soc Chang 74(7):887–935, 2007.

Riahi K, Krey V, Rao S, Chirkov V, Fischer G, Kolp P, Kindermann G, Nakicenovic N, Rafai P.: RCP-8.5: exploring the consequence of high emission trajectories. Climatic Change. doi: 10.1007/s10584-011-0149-y , 2011.

Stavrakou, T., and J.-F. Müller, Grid-based vs. big-region approach for inverting CO emissions using Measurement of Pollution in the Troposphere (MOPITT) data, J. Geophys. Res., 111, D15304, doi:10.1029/2005JD006896, 2006.

Stavrakou, T., Müller, J.-F., Bauwens, M., De Smedt, I., Van Roozendael, M., Guenther, A., Wild, M. and Xia, X. : Isoprene emissions over Asia 1979-2012: impact of climate and land-use changes, Atmos. Chem. Phys., 14(9), 4587–4605, doi:10.5194/acp-14-4587-2014, 2014.

Stavrakou, T., J.-F. Müller, M. Bauwens, I. De Smedt, M. Van Roozendael, M. De Mazière, C. Vigouroux, F. Hendrick, M. George, C. Clerbaux, P.-F. Coheur, and A. Guenther, How consistent are top-down hydrocarbon emissions based on formaldehyde observations from GOME-2 and OMI? Atmos. Chem. Phys. Discuss., 15, 12007-12067, 2015.

Stier, P., Feichter, J., Kinne, S., Kloster, S., Vignati, E., Wilson, J., Ganzeveld, L., Tegen, I., Werner, M., Balkanski, Y., Schulz, M., Boucher, O., Minikin, A., and Petzold, A.: The aerosol-climate model ECHAM5-HAM, Atmos. Chem. Phys., 5, 1125–1156, 2005.

Worden, H. M., Deeter, M. N., Edwards, D. P., Gille, J. C., Drummond, J. R., and Nédélec, P.: observations of near-surface carbon monoxide from space using MOPITT multispectral retrievals, J. Geophys. Res., 115, D18314, doi:10.1029/2010JD014242, 2010.

Wunch, D., Toon, G. C., Blavier, J.-F. L., Washenfelder, R. A., Notholt, J., Connor, B. J., Griffith, D. W. T., Sherlock, V., and Wennberg, P. O.: The Total Carbon Column Observing Network, Phil. Trans. R. Soc. A, 369, doi:10.1098/rsta.2010.0240, 2011.

Zhang, K., O'Donnell, D., Kazil, J., Stier, P., Kinne, S., Lohmann, U., Ferrachat, S., Croft, B., Quaas, J., Wan, H., Rast, S., and Feichter,J.: The global aerosol-climate model ECHAM-HAM, version 2: sensitivity to improvements in process representations, Atmos. Chem. Phys., 12, 2012.

List of Acronyms

ACCMIP	The Atmospheric Chemistry and Climate Model Intercomparison Project
AERONET	Aerosol Robotic Network (aeronet.gsfc.nasa.gov)
AIRS	Atmospheric Infrared Sounder
AOD	Aerosol optical depth
BIRA	Belgian Institute for Space Aeronomy (www.aeronomie.be)
CCMI	Chemistry Climate Modelling Initiative (www.met.reading.ac.uk/ccmi)
CTM	Chemistry transport model
ECHAM-HAMMOZ	Aerosol climate model based on the climate model ECHAM
ECHAM/MESSy	Chemistry climate model based on the climate model ECHAM and the Modular Earth Submodel System
ECMWF	European Centre for Medium Range Weather Forecasts (www.ecmwf.int)
EO	Earth observation
FMI	Finnish Meteorological Institute (http://en.ilmatieteenlaitos.fi/)
FTIR	Fourier Transform Infra-Red (ground-based) observations
GFED4	Global Fire Emissions Database (version 4)

GMD	Geoscientific Model Development (http://www.geoscientific-model-development.net/)
GOSAT	Greenhouse Gases Observing Satellite
IASI	The Infrared Atmospheric Sounding Interferometer
IGAC	International Global Atmospheric Chemistry project (www.igacproject.org)
KIT	Karlsruhe Institute of Technology (www.kit.edu)
KNMI	Royal Netherlands Meteorological Institute (http://www.knmi.nl/over-het-knmi/about)
MACC/CAMS	Monitoring Atmospheric Composition & Climate / Coperrnicus Atmospheric Monitoring System
MEGAN	Model of Emissions of Gases and Aerosols from Nature
MOHYCAN	Biogenic Hydrocarbon Emission Modeling
MOPITT	Measurement of Pollution in the Troposphere
MPI BGC	Max Planck Institute for Biogeochemistry (www.bgc-jena.mpg.de)
NDACC	Network for the Detection of Atmospheric Composition Change (www.ndacc.org)
SOA	Secondary Organic Aerosol
TCCON	Total Carbon Column Observing Network (www.tccon.caltech.edu)
VOC	Volatile Organic Compounds
WCRP	World Climate Research Programme (wcrp-climate.org)